Subhalo destruction in the APOSTLE and AURIGA simulations

Jack Richings[1,2⋆], Carlos Frenk[1], Adrian Jenkins[1], Andrew Robertson[1], Azadeh Fattahi[1], Robert J. J. Grand[3], Julio Navarro[4], Rüdiger Pakmor[3,5] Facundo A. Gomez[3,7], Federico Marinacci[8,9], Kyle Oman[1,4,10]

[1] *Institute for Computational Cosmology, Department of Physics, University of Durham, South Road, Durham DH1 3LE, UK*
[2] *Institute for Particle Physics Phenomenology, Department of Physics, University of Durham, South Road, Durham DH1 3LE, UK*
[3] *Max-Planck-Institut fur Astrophysik, Karl-Schwarzschild-Str. 1, D-85748 Garching, Germany*
[4] *Department of Physics and Astronomy, University of Victoria, PO Box 3055 STN CSC, Victoria, BC, V8W 3P6, Canada*
[5] *Heidelberger Institut fur Theoretische Studien, Schloss-Wolfsbrunnenweg 35, 69118 Heidelberg, Germany*
[6] *Instituto de Investigacion Multidisciplinar en Ciencia y Tecnologia, Universidad de La Serena, Raul Bitran 1305, La Serena, Chile*
[7] *Departamento de Fisica y Astronomia, Universidad de La Serena, Av. Juan Cisternas 1200 N, La Serena, Chile*
[8] *Kavli Institute for Astrophysics and Space Research, Massachusetts Institute of Technology, Cambridge, MA 02139, USA*
[9] *Harvard-Smithsonian Center for Astrophysics, 60 Garden Street, Cambridge, MA 02138, USA*
[10] *Kapteyn Astronomical Institute, University of Groningen, Postbus 800, NL-9700 AV Groningen, The Netherlands*

7 December 2019

ABSTRACT

N-body simulations make unambiguous predictions for the abundance of substructures within dark matter halos. However, the inclusion of baryons in the simulations changes the picture because processes associated with the presence of a large galaxy in the halo can destroy subhalos and substantially alter the mass function and velocity distribution of subhalos. We compare the effect of galaxy formation on subhalo populations in two state-of-the-art sets of hydrodynamical ΛCDM simulations of Milky Way mass halos, APOSTLE and AURIGA. We introduce a new method for tracking the orbits of subhalos between simulation snapshots that gives accurate results down to a few kiloparsecs from the centre of the halo. Relative to a dark matter-only simulation, the abundance of subhalos in APOSTLE is reduced by 50% near the centre and by 10% within r_{200}. In AURIGA the corresponding numbers are 80% and 40%. The velocity distributions of subhalos are also affected by the presence of the galaxy, much more so in AURIGA than in APOSTLE . The differences on subhalo properties in the two simulations can be traced back to the mass of the central galaxies, which in AURIGA are typically twice as massive as those in APOSTLE . We show that some of the results from previous studies are inaccurate due to systematic errors in the modelling of subhalo orbits near the centre of halos.

Key words: cosmology: theory – cosmology: dark matter – methods: N-body simulations – galaxies: kinematics and dynamics

1 INTRODUCTION

In the Λ-Cold Dark Matter (ΛCDM) model of cosmology, the formation of cosmic structure proceeds hierarchically by the merging of smaller structures to form larger ones (Peebles 1980; Davis et al. 1985). Whilst the merging process is incomplete, substructures can survive within the dark matter halo of a galaxy or cluster (Ghigna et al. 1998). In galaxies like the Milky Way many more such substructures survive than there are visible satellites (Moore et al. 1999; Klypin et al. 1999). This disparity is the natural outcome of physical processes known to be important in galaxy formation: the reionization of hydrogen around redshift $z = 8$ (Planck Collaboration et al. 2016) and the expulsion of gas heated by supernovae (Bullock et al. 2000; Benson et al. 2002; Somerville 2002; Okamoto et al. 2008; Sawala et al. 2016; Macciò et al. 2010). Similarly, an apparent absence of visible galaxies in the most massive subhalos that form in ΛCDM dark-matter-only simulations (Boylan-Kolchin et al. 2011) can be readily explained by processes related to gas expulsion from subhalos at early times (Sawala et al. 2013, 2016).

Even though baryon effects are sufficient to account for the abundance of galactic satellites within the standard ΛCDM model, a number of alternative models for the nature of the dark matter have been proposed motivated largely by a desire to explain these so-called "missing satellites" and "too-big-to-fail" problems. (e.g Spergel & Steinhardt 2000; Colín et al. 2000; Petraki & Volkas 2013; Schewtschenko et al. 2015; Hui et al. 2017). With a judicious choice of the additional parameters in these alternative models, e.g. the mass of a warm dark matter (WDM) particle, the abundance of satellites in the Milky Way can also be reproduced (Lovell et al. 2012, 2017). A particularly interesting WDM candidate is motivated by the discovery of a 3.5 keV emission line in the X-ray

⋆ Contact e-mail: jack.richings@durham.ac.uk

Downloaded from https://academic.oup.com/mnras/advance-article-abstract/doi/10.1093/mnras/stz3448/5679897 by University of Durham user on 03 January 2020

spectra of galaxies and clusters (Bulbul et al. 2014; Boyarsky et al. 2014). Whilst the nature of the origin of this line is disputed (Malyshev et al. 2014; Anderson et al. 2015; Jeltema & Profumo 2015; Franse et al. 2016; Riemer-Sørensen 2016), if its origin is not explicable within the standard model of particle physics, it could be the result of the decay of 7 keV sterile neutrino dark matter.

A key prediction that distinguishes CDM from some of the alternatives, such as WDM, is the abundance of small-mass halos and subhalos. In CDM, the halo mass function continues to rise to small masses (Diemand et al. 2007; Springel et al. 2008), whereas in WDM, the halo mass function is truncated at a mass on the scale corresponding to dwarf galaxies (Colín et al. 2000; Lovell et al. 2012; Schneider et al. 2012; Hellwing et al. 2016; Bose et al. 2017). In sterile neutrino models, the power spectrum of primordial fluctuations depends not only on the dark matter particle mass but also on an additional lepton asymmetry parameter. In the coldest sterile neutrino model compatible with the 3.5 keV line originating from particle decay, the mass function is suppressed by a factor of 5 relative to CDM at 10^8 $\mathrm{M}_\odot$ and is negligible at 10^7 $\mathrm{M}_\odot$ (Bose et al. 2017). Thus, detection of halos of mass below 10^7 $\mathrm{M}_\odot$ would rule out this candidate particle and set a lower limit larger than 7 keV for the sterile neutrino mass. Conversely, a convincing non-detection of halos of mass below $\sim 10^8$ $\mathrm{M}_\odot$ would rule out CDM (Li et al. 2016).

If they exist, the vast majority of these small-mass halos will be dark, that is, almost completely devoid of baryonic matter. This baryon deficit is the result of reionisation and supernova heating (Okamoto et al. 2008; Sawala et al. 2016). These dark objects can be detected through their gravitational interaction with visible matter. A particularly promising test is gravitational imaging (Koopmans 2005) in which low-mass halos perturb the giant arcs or Einstein rings that can be produced when a background galaxy is strongly lensed. This method has already yielded detection of a $1.9 \pm 0.1 \times 10^8$ $\mathrm{M}_\odot$ dark satellite and, with imaging data of good quality, the detection sensitivity could reach 2×10^7 $\mathrm{M}_\odot$ (Vegetti et al. 2012)[1].

Although for practical lensing configurations the lensing signal is dominated by field halos rather than subhalos (Li et al. 2017; Despali et al. 2018), the latter make a non-negligible contribution to the lensing distortion. Since dark subhalos in this low-mass range are uncontaminated by baryonic matter at the present day, the only uncertainty in their abundance arises from possible interactions between subhalos and the central galaxy in their common host halo, for example tidal disruption. Quantifying these effects is necessary to make accurate predictions for the expected lensing signals.

The abundance of dark substructure in our own Galaxy may be probed in other ways. For example, stellar streams, formed by the tidal disruption of globular clusters or dwarf galaxies, can be measurably perturbed by passing substructures which produce gaps in the streams (Carlberg et al. 2012). Surveys such as GAIA (Perryman et al. 2001; Gilmore et al. 2012), DES (The Dark Energy Survey Collaboration 2005), and LSST (LSST Science Collaboration et al. 2009) have the potential to measure these gaps and thereby determine the mass function of substructures in the Milky Way down to a scale of $10^7 \mathrm{M}_\odot$ (Erkal & Belokurov 2015b,a). Such methods were explored in Erkal et al. (2016); their results are affected by a number of uncertainties, as the simulations used did not incorporate baryonic physics, and a particular velocity distribution of subhalos was assumed to break the degeneracy in the method between peturber mass and velocity.

The role of the central galaxy in the destruction of substructure has been studied using N-body simulations that incorporate an analytic disk potential (D'Onghia et al. 2010; Yurin & Springel 2015), as well as hydrodynamical simulations (Garrison-Kimmel et al. 2017; Sawala et al. 2017). The specific implementation of baryonic physics is important: the choice of subgrid model, physical parameters and method for solving the hydrodynamical equations all individually can affect the abundance of substructure. Errani et al. (2017) also showed that the inner slope of the density profile of infalling substructures affects their survival probability. Benitez-Llambay et al. (2018) showed that the central density of dwarf galaxies depends strongly on the choice of the star formation gas density threshold, a CDM cosmological simulation producing cuspy or cored profiles depending on the choice of this parameter.

The effect of changing the subgrid galaxy formation models on subhalo abundance has been investigated by Despali & Vegetti (2017) in the case of the EAGLE and ILLUSTRIS 100^3 Mpc^3 simulations (Schaye et al. 2015; Vogelsberger et al. 2014). Both simulations have relatively poor mass resolution (approximately 10^7 $\mathrm{M}_\odot$) so this study was restricted to massive substructures rather than the small ones that are important for distinguishing CDM from WDM. Furthermore, the outputs of these simulations are sufficiently infrequent that the destruction of subhalos in the innermost regions of galaxies, where processes such as disk shocking are important, is poorly sampled.

With mass resolution of approximately 10^4 $\mathrm{M}_\odot$, the simulations that we analyze in this paper have at least 100 times better resolution than the simulations studied by Despali & Vegetti (2017). In particular, they resolve the small-mass halos (mass $\sim 10^7$ $\mathrm{M}_\odot$) required to distinguish CDM from WDM. To investigate the dependence of the surviving subhalo abundance on the choice of baryonic physics implementation, we compare the APOSTLE (Sawala et al. 2016; Fattahi et al. 2016) and AURIGA (Grand et al. 2016) CDM simulations. We integrate the orbits of subhalos between snapshots to obtain precise estimates of time-averaged subhalo abundance close to the centre of the halo. This is the first direct comparison of baryonic physics models at such a high level of resolution, both spatially and temporally.

2 METHODS

2.1 Simulations

We use two suites of simulations to study the impact of baryons on galactic substructure. The first is a set of zoom simulations of Local Group-like volumes from the APOSTLE project (Fattahi et al. 2016; Sawala et al. 2016). Each volume contains a pair of halos, each of mass $\sim 10^{12}$ $\mathrm{M}_\odot$, corresponding to the Milky Way and Andromeda. We study the same two volumes considered by Sawala et al. (2017), giving a total of four high-resolution halos. The second suite of simulations, taken from the AURIGA project (Grand et al. 2016), is a set of zoom simulations of individual Milky-Way sized galaxies, selected from the EAGLE 100^3 Mpc^3 simulation (L0100N1504) (Schaye et al. 2015). There are six high-resolution ("level 3") halos in the AURIGA sample. In addition, in § 3.1 we also analyze the larger , "level 4", sample of 30 halos simulated at 10 times lower mass resolution than the level 3 examples.

[1] The definition of mass here is based on a pseudo-Jaffe model and differs from the standard definition of halo and subhalo masses used in cosmological simulations and in this paper.

Downloaded from https://academic.oup.com/mnras/advance-article-abstract/doi/10.1093/mnras/stz3448/5679897 by University of Durham user on 03 January 2020

For each simulation we have both a dark matter only (DMO) version and a version including baryonic physics relevant to galaxy formation (gas cooling, star formation, chemical enrichment, black hole formation, feedback from stellar evolution, AGN, etc.) The APOSTLE simulations were performed with with the EAGLE reference model (Schaye et al. 2015; Crain et al. 2015), which is based on Gadget3, while the AURIGA simulations were performed with a variant of the Arepo code (Springel 2011; Grand et al. 2016) used for the ILLUSTRIS simulation (Vogelsberger et al. 2014). The parameters of the subgrid models in EAGLE and ILLUSTRIS are calibrated somewhat differently. In EAGLE, they are chosen so as to reproduce the $z = 0$ galaxy stellar mass function and size distribution, while in ILLUSTRIS they are tuned to match the $z = 0$ ratio of galaxy stellar to dark matter mass and the cosmic star formation rate at all times. Key diagnostics of each halo, as well as relevant simulation parameters are listed in Table 1.

The main halos in the APOSTLE and AURIGA simulations have broadly similar masses, $\sim 10^{12}$ M$_\odot$; however, the stellar masses of the central galaxies in AURIGA are significantly larger, typically around twice as massive as an APOSTLE galaxy. The AURIGA galaxies are also more concentrated than the APOSTLE galaxies; despite being twice as massive, their half-stellar-mass radii are similar or smaller than those of APOSTLE galaxies.

All quantities in this paper are averaged over the 5 Gyr period, between redshift $z = 0.5$ and the present day, to give an expected probability density over this time interval. In both simulations, halos are identified using the friends-of-friends algorithm (Davis et al. 1985). Halo substructure is identified using the SUBFIND algorithm (Springel et al. 2001). When computing averages over multiple halos, we take the median value in physical units. In Table 1 and throughout this work we adopt the common measures r_{200} and M_{200} to define the size and mass of the host halos respectively. r_{200} is defined as the radius within which the mean mass density is 200 times the critical density of the Universe. M_{200} is the total mass enclosed within that radius. When performing time-averaged calculations which span several snapshots, we interpolate r_{200} and M_{200} linearly in time.

2.2 Halo masses

In DMO simulations, the baryonic mass is collisionless: around 15% (the value of Ω_b/Ω_m) of the mass of each simulation particle represents "collisionless baryons". In hydrodynamical simulations, low-mass halos lose much of their baryonic mass during reionisation or, subsequently, through galactic winds powered by supernovae. DMO halos cannot undergo this mass loss, and so they will be approximately 15% more massive than their hydrodynamical counterparts at early times. This difference in mass is exacerbated with time because more massive halos accrete mass at a higher rate than smaller mass halos and thus grow faster. For an isolated 10^8 M$_\odot$ halo at redshift $z = 0$, this difference in mass between the same object with hydrodynamics or DMO is typically around 20-30% (Sawala et al. 2013, 2016).

Most of the results presented in this work do not include a correction for this effect. This is largely in order to make it easier to compare with previous studies based on DMO simulations. However, if we wish to identify what fraction of the reduction in halo abundance is attributable to interactions with the host galaxy rather than to this environmentally-independent mass loss effect, it is necessary to correct the mass of DMO halos. We use this correction for some of the calculations presented in § 3.1.

The procedure we use to correct DMO halo masses is as follows. We match halos between the DMO and hydrodynamical versions of a simulation using the particle matching criterion of Bose et al. (2017), in which the 50 most bound DM particles of halos are matched bijectively between the DMO and hydrodynamical simulations. We then form a matched "field" sample by selecting halos which are at least 500 kpc from a galaxy in the hydrodynamical version of the simulation, so as to avoid any differences due to evolution in the tidal field of the main halo. For each AURIGA level 3 volume, we have approximately 1000 matched objects with mass between 10^7–10^8 M$_\odot$. The numbers for APOSTLE are significantly larger as a greater fraction of the simulation is field volume. For each pair of matched halos we calculate the ratio of their masses. We take a DMO halo's "effective mass" to be the mass assigned to it by the SUBFIND algorithm, multiplied by the median of the distribution of mass ratios of this matched sample. The distributions of mass ratios before and after this procedure are shown in Fig. 1. When the masses of DMO subhalos are corrected by the median mass ratio, the peak of the mass ratio distribution will occur at a value of 1, by construction (this would not be the case if we had corrected by the mean mass ratio). The width of the corrected distribution is around 30% larger for the corrected distribution. The results shown in Fig. 1 are calculated using only subhalos at redshift $z = 0$. We have checked that for redshifts between $z = 1$ and the present day, the size of this effect is independent of redshift.

We find that the correction factor has no dependence on mass for halos with DMO masses between $10^7 - 10^9$ M$_\odot$. For the AURIGA simulations, we find a median correction factor of 0.76, and the interquartile range of of correction factors is 0.12. For the APOSTLE simulations the median correction factor is 0.75, due to the slightly different choice of cosmological parameters in the simulation. We find that this correction procedure does not work well for halos with masses below 10^7 M$_\odot$. The probability of a halo being matched between simulations falls steeply for halos smaller than this. Furthermore, the distribution of mass ratios will be biased as the resolution limit of the simulation imposes a limit on the smallest possible mass ratio. Therefore, when correcting halo masses, we restrict our attention to halos with masses greater than 10^7 M$_\odot$.

2.3 Orbits

The time between snapshots in the simulations (around 300 Myr for APOSTLE and less for AURIGA) is greater than the crossing time for the central 20-30 kpc of the main halo. These snapshots are sufficiently infrequent that the subhalo abundance in the central 20 kpc of the halo is poorly sampled. To make precise theoretical predictions for the abundance of substructure near the centre of halos and to quantify the impact of the galactic disk, previous studies inferred the positions of subhalos between snapshots using a cubic spline to interpolate between snapshots (Sawala et al. 2017; Garrison-Kimmel et al. 2017). Specifically, a cubic piecewise polynomial was fit to each Cartesian coordinate of the physical positions of subhalos at the snapshots as a function of time with the condition that the result be twice continuously differentiable, except at the ends, where the first derivative is equal to the linear interpolant slope.

We show in §2.3.1 that this method is biased. Cubic spline interpolation systematically underpredicts the orbital radii of subhalos at distances of less than 30 kpc from the centre of the halo,

Downloaded from https://academic.oup.com/mnras/advance-article-abstract/doi/10.1093/mnras/stz3448/5679897 by University of Durham user on 03 January 2020

	M_{200} [$10^{12} M_\odot$]		N_{sub}		M_{gal} [$10^{10} M_\odot$]	m_{DM} [$10^4 M_\odot$]	Softening [kpc]
	DMO	Hydro	DMO	Hydro			
APOSTLE - 11	1.66	1.57	2027	1543	3.40	4.92	0.13
APOSTLE - 12	1.10	1.02	2158	1563	1.87	4.92	0.13
APOSTLE - 41	1.35	1.16	1579	1253	1.11	2.45	0.13
APOSTLE - 42	1.39	1.12	2650	1675	1.94	2.45	0.13
AURIGA - 6	1.05	1.01	1355	675	7.30	3.64	0.18
AURIGA - 16	1.49	1.50	2088	936	9.28	3.89	0.18
AURIGA - 21	1.51	1.42	2094	932	11.23	4.11	0.18
AURIGA - 23	1.61	1.50	1870	915	10.45	4.35	0.18
AURIGA - 24	1.50	1.47	1982	943	9.12	3.92	0.18
AURIGA - 27	1.76	1.70	2351	1021	10.99	4.03	0.18

Table 1. Properties of the halos analyzed in this work at redshift $z = 0$. Each AURIGA halo is the largest object identified using the friends-friends-algorithm. Each APOSTLE halo is either the largest or second largest friends-of-friends group. N_{sub} is the number of subhalos identified by the SUBFIND algorithm (Springel et al. 2001), with mass greater than $10^{6.5}$ $M_\odot$, inside r_{200}; M_{gal} is the total mass of all gas and star particles within 30 kpc from the centre of the halo; m_{DM} is the mass of the high-resolution dark matter particle used in the hydrodynamical simulations. The softening is the value appropriate to the high-resolution dark matter particles at redshift $z = 0$.

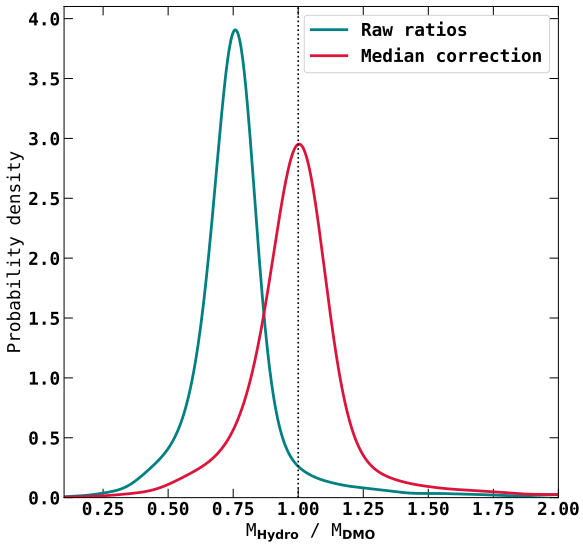

Figure 1. Distribution of the ratios of the masses of halos matched between DMO and hydrodynamical versions of a simulation. The teal line shows the distribution of mass ratios when no correction has been applied. The crimson line shows the distribution of mass ratios after the masses of DMO halos have been multiplied by the median of the teal distribution (a value of 0.76).

precisely the region where reconstructing subhalo orbits is most important for tests of the CDM model. Orbital radii are often underpredicted by a factor of two or more, especially if pericentre occurs at a time halfway between two snapshots.

Instead of interpolating, we track the positions and velocities of subhalos between snapshots by integrating their orbits in the potential of the halo, which we assume to be static over this time and, for simplicity, axisymmetric. We model the potential and integrate the orbits using the publicly available codes GALPY and PYNBODY (Bovy 2015; Pontzen et al. 2013). This method accurately reproduces the orbits of subhalos around the host halo, even in situations where the cubic spline method is most prone to failure. By integrating the orbits of subhalos we can accurately estimate subhalo abundances at galactic distances of less than 10 kpc.

To predict the position of a subhalo accurately, choosing the correct frame of reference is paramount. Following the prescription of Lowing et al. (2011) we take the coordinate origin of the halo to be the position of the particle with the minimum potential energy, and the velocity of the parent halo (which is to be subtracted from the velocity of the subhalo under consideration) to be the mean velocity of all particles within 5% of r_{200}. We define this reference frame for each snapshot. All calculations are performed in physical coordinates.

We match subhalos between snapshots using a merger tree. To determine the position and velocity of a subhalo between snapshots 1 and 2, in the time interval $t_1 < t < t_2$, we take the following steps:

(i) Construct an intermediate "snapshot" by summing the mass distributions of snapshots 1 and 2, halving the mass of each particle.

(ii) Since the required GALPY routines are written for axisymmetric potentials, we interpolate the mass distribution of the intermediate snapshot on a 2-dimensional $R-z$ grid[2]. We discard particles which are further than 800 kpc from the centre of the halo. The effect of this approximation on the calculated orbits is negligible. The z-axis of the grid is taken to be the z-direction in simulation coordinates, and so is unrelated to the plane of the galaxy. The accuracy of the results in Fig. 2 shows that this arbitrary choice of z-axis is unimportant as the mass distribution is close to spherical.

(iii) Taking the subhalo at snapshot 1 to be a point mass, integrate its orbit forwards in time in the intermediate potential using the standard GALPY fourth-order symplectic integrator.

(iv) Integrate the orbit of the subhalo at snapshot 2 backwards in time in the intermediate potential.

(v) The orbit of the subhalo is found by taking a weighted sum

[2] R is the two-dimensional cylindrical radius, and z is the vertical distance.

Downloaded from https://academic.oup.com/mnras/advance-article-abstract/doi/10.1093/mnras/stz3448/5679897 by University of Durham user on 03 January 2020

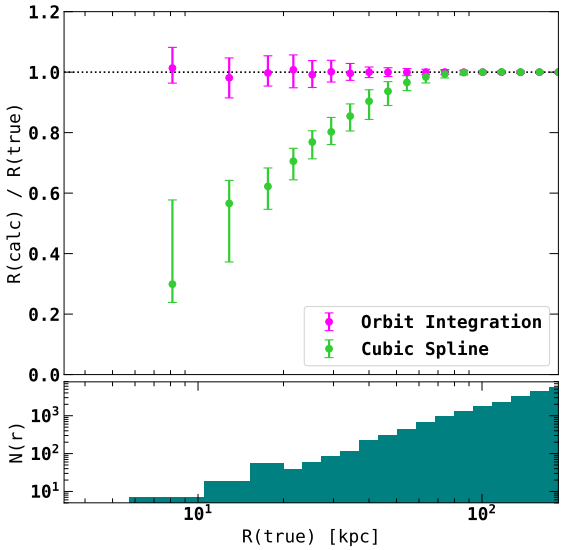

Figure 2. The accuracy of orbit integration at predicting the orbital radii of subhalos at an intermediate snapshot. For reference, we compare this method to the cubic spline described in Sawala et al. (2017) and also used in Garrison-Kimmel et al. (2017). The lower panel shows the number of subhalos present in each radial bin.

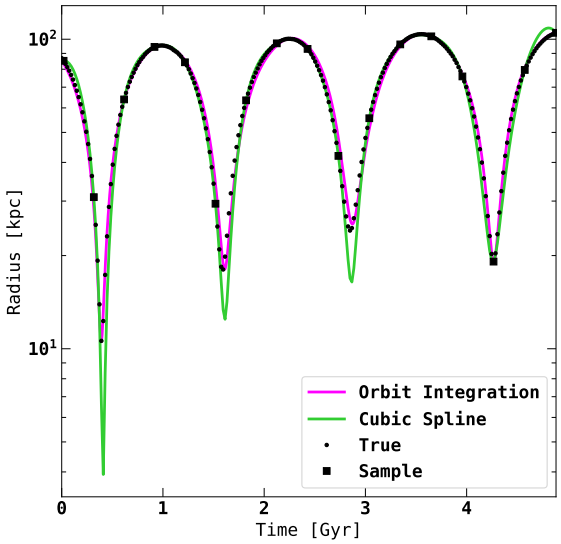

Figure 3. The distance of a subhalo from the halo centre of potential over several orbital periods in the Aquarius Aq-A4 simulation. Black circles show the distance measured at each snapshot. Black squares show the distance at snapshots used for orbit integration and fitting cubic splines. The pink line shows the orbit calculated using the orbit integration method described above. The green line shows the orbit inferred from the cubic spline method introduced by Sawala et al. (2017).

of the forwards and backwards orbits. The position, $\vec{x}$, of a subhalo at a time t in the interval $t_1 < t < t_2$ is given by:

$$\vec{x}(t) = \vec{x}_f(t)\frac{t_2 - t}{t_2 - t_1} + \vec{x}_b(t)\frac{t - t_1}{t_2 - t_1}, \quad (1)$$

where $\vec{x}_f$ and $\vec{x}_b$ are the positions of the subhalos being integrated forward and backward in time at time t respectively.

(vi) The position and velocity of each subhalo is output every 3 Myr.

To assess the accuracy of the reconstruction of subhalo orbits we perform the following experiment. We select a pair of non-consecutive snapshots from the AURIGA simulation (snapshots 99 and 101, corresponding to a redshift of $z \simeq 0.4$). The time between these snapshots is approximately the same as the time between successive APOSTLE snapshots. Using our method, we calculate the positions of all subhalos at the time of snapshot 100, which we can compare directly with the actual positions calculated at the intermediate snapshot. The results of this test are shown in Fig. 2. We can see that orbit integration accurately predicts the positions of subhalos between snapshots, and is therefore an effective tool for studying the dynamics of substructure close to the centre of the halo. The green points in Fig. 2 show the results of the same test when applied to subhalo orbits calculated using the cubic spline method. A detailed study of why the cubic spline method underpredicts the orbital radii of subhalos is given in the following subsection.

2.3.1 *Comparison to cubic spline*

To demonstrate the inaccuracies introduced by cubic spline interpolation, we use the AQUARIUS simulations. The AQUARIUS project is a set of DMO zoom-in simulations of 10^{12} $M_\odot$ dark matter halos (Springel et al. 2008). Specifically, we use the Aq-A4 simulation, which has 258 snapshots between $z = 0.5$ and the present day, and a high-resolution particle mass of 3.9×10^5 $M_\odot$. This time resolution is approximately sixteen times better than in the APOSTLE simulations. We select a subset of snapshots with the same temporal spacing as the snapshots in the APOSTLE simulations. We can compare the orbits calculated using the cubic spline interpolation on the subset of snapshots to the orbit measured in the additional snapshots not used to fit the cubic splines. Fig. 3 demonstrates how the cubic spline interpolation underestimates the orbital radius of a subhalo near pericentre. This underestimation occurs at pericentre as this is where the acceleration experienced by the subhalo is varying most rapidly. The cubic spline, which assumes that the acceleration of the subhalo is linear in time between snapshots, is unable to account for the rapidly varying force acting on the subhalo as its distance from the centre of the halo changes rapidly. In Fig. 4 we show a two-dimensional projection of the orbit over seven snapshots. The positions plotted for the cubic spline are calculated at the exact time of the AQUARIUS snapshots, so any deviations are due solely to the choice of interpolation.

In contrast, integrating the orbits of subhalos consistently reproduces the radius and time of pericentre passage with a high degree of accuracy, as seen in Figs. 3 and 4 .The orbit of the subhalo is determined by the shape of the potential and its current position and velocity. Integrating the orbits ensures that the relevant physics is included, leading to accurate predictions for the positions and velocities of subhalos between snapshots. On the other hand, the cubic spline interpolation method has no physical basis, leading to orbits which do not conserve angular momentum.

To quantify the error introduced by the cubic spline interpolation on the calculation of the subhalo radial distribution, we calculate the time-averaged cumulative radial distribution of subhalos over a 5 Gyr period using the positions in the AQUARIUS snapshots

Downloaded from https://academic.oup.com/mnras/advance-article-abstract/doi/10.1093/mnras/stz3448/5679897 by University of Durham user on 03 January 2020

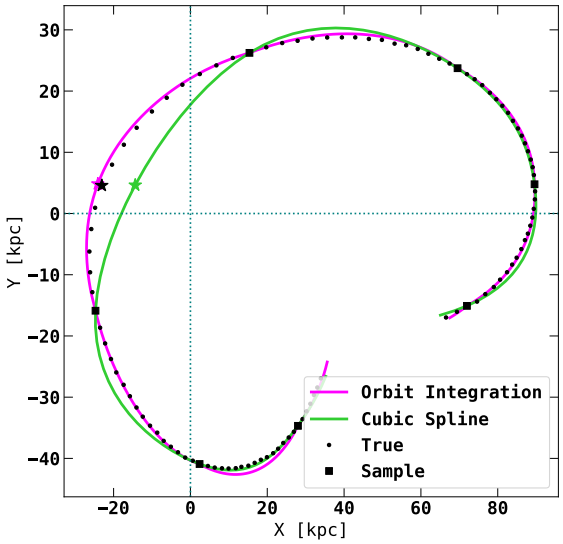

Figure 4. A two-dimensional projection of a portion of the subhalo orbit shown in Fig. 3. The orbit is close to planar in the z coordinate. The portion of the orbit is chosen from the middle of the whole orbit shown in Fig. 3 to prevent edge effects in the cubic spline interpolation. Black circles show the position of the subhalo at each snapshot, and black squares the position of the subhalo at the snapshots used to calculate the pink (orbit integration) and green (cubic spline) lines. Stars show the position of the pericentre of the orbit. The black star is almost exactly on top of the pink star.

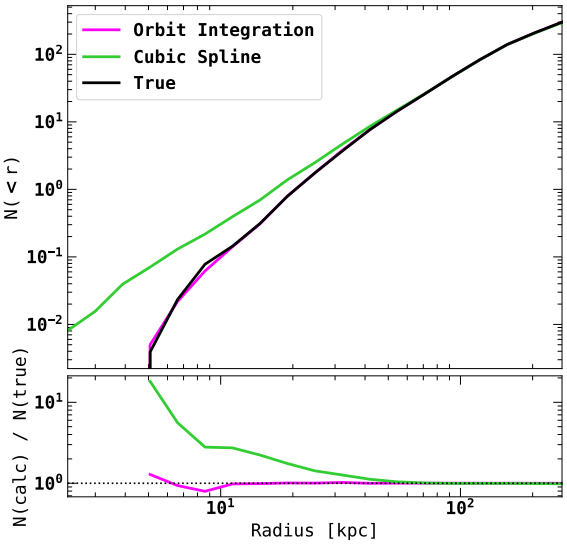

Figure 5. Cumulative radial distribution of subhalos, averaged over a 5 Gyr period, calculated using orbit integration (pink) and cubic spline interpolation (green) on a subset of simulation snapshots. The black line shows the radial distribution of subhalos measured using all snapshots. The bottom panel shows the ratio of the calculated and true number of subhalos inside a given radius.

and the positions calculated using either the cubic spline interpolation or our orbit integration method. Fig. 5 shows that the tendency of the cubic spline to underestimate the orbital radius of a subhalo leads to a large overprediction of the abundance of subhalos at radii less than 20 kpc (around 10% of r_{200}). At distances of less than 5 kpc from the halo centre, the cubic spline interpolation method predicts a significant chance of observing substructure despite no object having ever passed so close to the halo centre. By contrast, the orbit integration method matches the actual radial distributions perfectly.

3 ABUNDANCE OF SUBSTRUCTURE IN HYDRODYNAMICAL SIMULATIONS

The central galaxies that form in the AURIGA simulations are significantly more massive than those that form in the APOSTLE simulations, even though they both have broadly similar halo masses. We show in this section that the mass of the galaxy has a marked effect on subhalo abundance, even at distances well beyond the edge of the galaxy. In Fig. 6 we compare the radial distribution of subhalos in the APOSTLE , AURIGA and DMO simulations. The effect of the larger AURIGA galaxies is to reduce the abundance of subhalos at all radii. We find that the size of the reduction depends strongly on radius but is broadly independent of mass for subhalos in the range $10^{6.5} - 10^{8.5}$ M$_\odot$, in agreement with the conclusions of Sawala et al. (2017).

The reduction in subhalo abundance as a function of radius is shown explicitly in Fig. 7. Fundamental tests of the CDM model, for example using stellar streams to search for substructure, are sensitive to substructure within 20 kpc of the centre of the halo (or equivalently $\sim 10\%$ of r_{200} for a Milky Way-sized halo). At these radii, the presence of the galaxy reduces the substructure abundance by 50% in the APOSTLE and by 80% in the AURIGA simulations relative to the DMO case. The APOSTLE simulations predict over twice as many dark (i.e. low-mass) substructures as the AURIGA simulations.

In Fig. 8 we show the cumulative subhalo mass functions in four spherical shells in the DMO and hydrodynamical versions of the APOSTLE and AURIGA simulations. Power-law fits to the differential mass functions have slopes between -1.8 and -1.9 in the two outermost shells, consistent with the findings of both Springel et al. (2008) and Sawala et al. (2017). At distances less than 20 kpc from the halo centre (top panels) we find that the slopes of the mass functions in the AURIGA hydrodynamical simulations are significantly shallower than the corresponding slopes in APOSTLE, suggesting that the implementation of baryonic physics in AURIGA leads to a more pronounced reduction of small-mass relative to high-mass halos. This is simply because less massive halos are more prone to tidal disruption, rather than any systematic difference between the orbital distributions of smaller and larger halos. We fit the median mass function in each radial bin with a power law using a non-linear least squares method. In the innermost radial bin the slope in the AURIGA hydrodynamical simulations is -1.4, whereas the slope in APOSTLE simulations is -1.7. Values for all power-law fits are listed in Table 2.

3.1 Subhalo abundance far from the central galaxy

As the distance from the central galaxy increases, the reduction in subhalo abundance caused by the inclusion of baryonic physics should asymptote to a constant value, at a radius where the tidal field of the central galaxy has no impact on the evolution of small

Downloaded from https://academic.oup.com/mnras/advance-article-abstract/doi/10.1093/mnras/stz3448/5679897 by University of Durham user on 03 January 2020

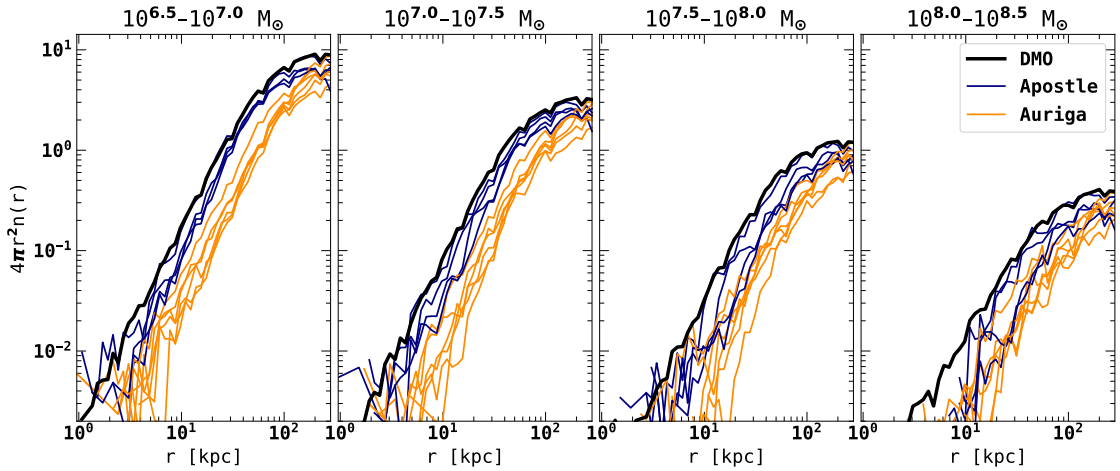

Figure 6. Linear density of subhalos in hydrodynamical and DMO versions of the APOSTLE (blue) and AURIGA (orange) simulations as a function of radius. The black line shows the median radial density of subhalos in all DMO simulations. Each panel corresponds to a different subhalo mass bin as indicated. The results are time averaged over a period of 5 Gyr.

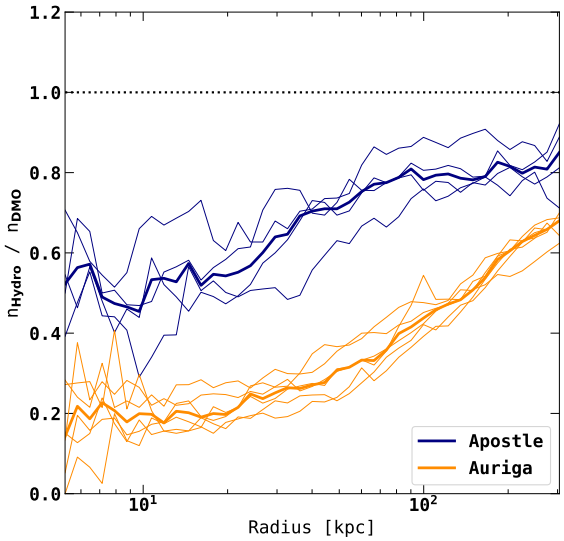

Figure 7. Ratio of the radial number density of subhalos in hydrodynamical and DMO versions of the APOSTLE (blue) and AURIGA (orange) simulations, for subhalos with masses in the range $10^{6.5} - 10^{8.5}$ M$_\odot$. Thin lines show the reduction in subhalo abundance for individual halos and the thick lines the median of the thin lines.

	0-10	10-20	20-50	50-200
Apostle DMO	-1.74	-1.88	-1.90	-1.91
Auriga DMO	-1.69	-1.77	-1.92	-1.93
Apostle Hydro	-1.73	-1.86	-1.92	-1.93
Auriga Hydro	-1.44	-1.64	-1.82	-1.94

Table 2. Power-law slopes for differential subhalo mass functions in the mass range $(10^{6.5} - 10^{8.5})$ M$_\odot$ in DMO and hydrodynamical simulations, in four spherical shells. The width of the spherical shell (top row) is given in kpc.

halos. This is indeed what we see in Fig. 7 which shows that the ratio of subhalo abundance in the hydrodynamical and DMO simulations rises with distance from the centre of the halo, until it begins to plateau at a radius of ~ 300 kpc. The reason that the lines in Fig. 7 do not plateau at a value of 1 is because we computed the number density of subhalos in fixed mass bins, without correcting for the effects described in §2.2. The radius at which the reduction in subhalo abundance plateaus to a constant value is significantly outside of r_{200}, which has a typical value of 220 kpc for the halos in our sample. Thus, the impact of the central galaxy seems to extend surprisingly far, well beyond the extent of the galactic disks. This conclusion is based on two observations.

Firstly, the velocity anisotropy of subhalos is lower (implying more circularly-biased orbits) in the hydrodynamical simulations compared to the DMO case. The difference in velocity anisotropy only becomes negligible at around 300 kpc. Secondly, the number of halos that have been in and out of the main halo is larger in the DMO than in the hydrodynamical simulations. To show this, we count the number of halos of mass $(10^7 - 10^8)$ M$_\odot$ in a spherical shell between 200 and 300 kpc. For each subhalo we check if it has previously been close to the central galaxy[3]. We find that the difference in the number of subhalos between the hydrodynamical and DMO simulations is strongly correlated with the difference in the number of subhalos that have been close to the centre of the halo. In other words, at large radii there exists a population of DMO subhalos that have fallen into the halo, survived their passage through the centre, and reemerged. These are sometimes called "splashback halos"; Gill et al. 2005. Many of their hydrodynamical counterparts do not survive the encounter with the galaxy at the centre of the halo, and so we observe the abundance ratio continuing to rise to distances of 300 kpc from the centre of the halo, well beyond r_{200}. The results of this calculation for the level 4 suite of AURIGA simulations (see §2) are shown in Fig. 9. Here we compare results with and without the mass correction described in §2.2. We see a clear

[3] We adopt a radius of $0.7\times r_{200}$ as our definition of 'close'. This is a typical radius at which the tidal forces from the spherically averaged mass distributions in the hydrodynamical simulations are equal to the tidal forces in the DMO simulations.

Downloaded from https://academic.oup.com/mnras/advance-article-abstract/doi/10.1093/mnras/stz3448/5679897 by University of Durham user on 03 January 2020

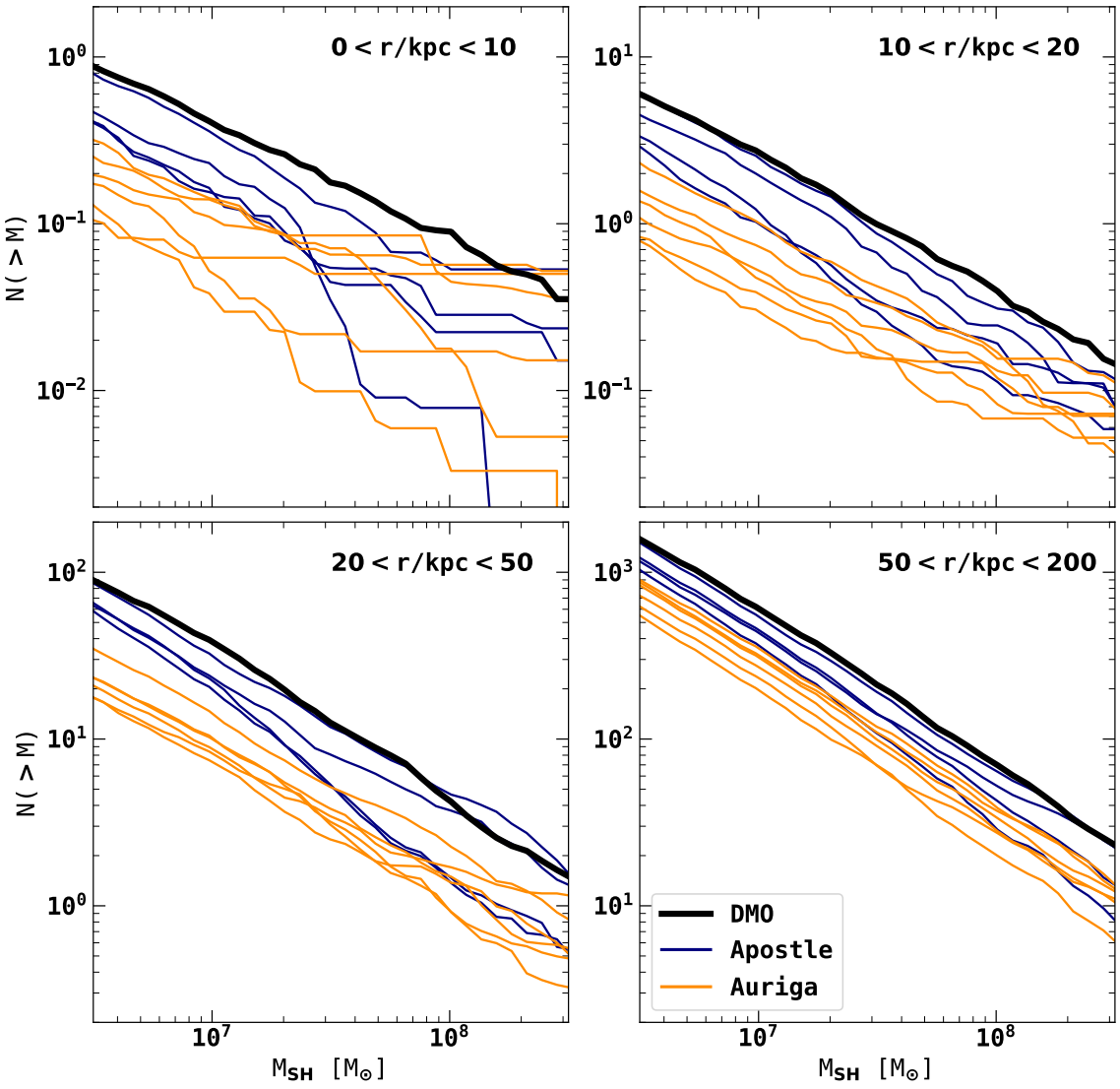

Figure 8. Cumulative subhalo mass functions for subhalos in the APOSTLE (blue) and AURIGA (orange) hydrodynamical simulations. Each panel represents a different spherical shell. The thick black lines show the median cumulative subhalo mass function of all APOSTLE and AURIGA DMO subhalos in each radial bin.

correlation in both cases; however, when the mass correction is applied, the points fall roughly along the expected 1:1 line.

To explore this point further, we compare the evolution of a population of subhalos matched between the DMO and hydrodynamical simulations. We match the subhalos firstly by particle IDs, using the matching criterion of Bose et al. (2017) and, secondly, by requiring that the subhalos should have the same mass and distance from the centre of the main halo to within 10%. These criteria is quite restrictive, and effectively limits our sample to objects which have not yet had an interaction with the main halo yet. Matched objects have the same orbits at redshift $z = 1$, so we can confidently attribute present day differences between the matched objects to interactions that occur during the time period we study. We track the masses and positions of our matched sample between redshift $z = 1$ and the present day, a period of roughly 8 Gyr, and compare matched subhalos that were between 200 and 300 kpc from the centre of the halo at redshift $z = 1$. From this sample we select objects that ceased to exist before redshift $z = 0$ in the hydrodynamical version but that survive to the present day in the DMO version. Subhalos that meet these criteria are approximately three times as common as subhalos that survive in the hydrodynamical simulation but are destroyed in the DMO simulation.

Downloaded from https://academic.oup.com/mnras/advance-article-abstract/doi/10.1093/mnras/stz3448/5679897 by University of Durham user on 03 January 2020

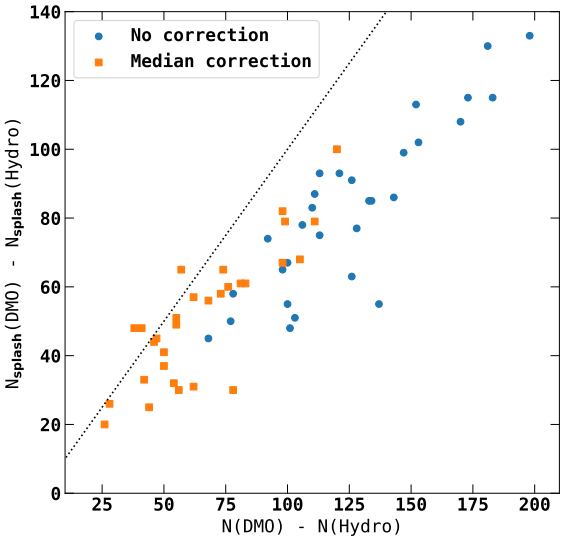

Figure 9. Difference in the number of subhalos with masses in the range (10^7-10^8) $M_\odot$ in a spherical shell of width 200–300 kpc in the DMO and hydrodynamical simulations plotted against the difference in the number of subhalos in this shell that have previously been inside 70% of r_{200} (labelled by the subscript *splash*). Each point represents a halo from the level 4 AURIGA suite of simulations. The blue points show the halos where we have not applied any correction to the masses of DMO subhalos. The orange points show the result when we correct the masses of DMO subhalos using the mass correction technique described in §2.2.

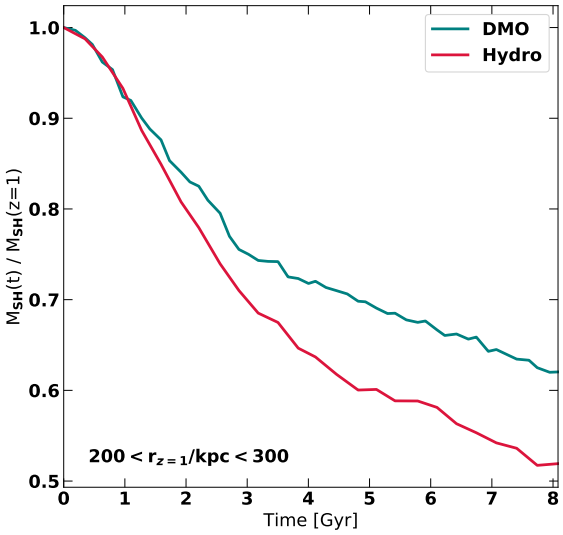

Figure 10. Mass loss of subhalos between redshift, $z = 1$, and the present day for a sample of subhalos matched between DMO and hydrodynamical versions of the AURIGA simulations. Subhalos are selected at $z = 1$ to be between 200-300 kpc from the centre of the main halo and to have a mass in the range $(10^{6.5} - 10^{8.5})$ $M_\odot$. Each line shows the median reduction in mass as a function of time for subhalos which survive to the present day.

We can also use our matched sample of subhalos to assess the role of mass stripping (rather than complete destruction) in the reduction in subhalo abundance. The steepness of the subhalo mass function means that it is possible to measure a reduction in subhalo abundance in a particular mass bin, if subhalos undergo significant stripping without any destruction taking place at all. We select a sample of matched subhalos that lie between 200 and 300 kpc from the centre of the halo at $z = 1$, have a mass in the DMO simulation in the range $(10^{6.5} - 10^{8.5})$ $M_\odot$ and survive to the present day. Although we do not specify it in advance, we find that the dynamics of these matched objects, specifically their average distance from the centre of the main halo as a function of time, is identical in the hydrodynamical and DMO samples. Fig. 10 shows the median reduction in subhalo mass as a function of time. DMO subhalos lose an average of 38% of their mass, whilst subhalos in AURIGA lose an average of 49%. Thus, a halo in the hydrodynamical simulation with the same initial mass as its DMO counterpart at redshift $z = 1$ will be, on average, about 20% less massive today, even if it shares the same radial distance history. This merely reflects the enhanced tidal stripping in the latter case due to the presence of the massive central galaxy. We can quantify the contribution of this effect to the overall reduction in abundance as follows.

We assume a power-law mass function of the form,

$$\frac{dN}{dM_0} = kM_0^\alpha \ , \tag{2}$$

where M_0 is the uncorrected mass. The mass of the subhalo after stripping is given by $M_1 = \beta M_0$. Thus,

$$\frac{dN}{dM_1} = k\beta^{-\alpha-1}M_1^\alpha \ , \tag{3}$$

so the ratio of the mass functions is given by $\beta^{-\alpha-1}$. Taking values of $\alpha = -1.9$ for the power law slope of the subhalo mass function(Springel et al. 2008), and $\beta = 0.8$ for the stripping factor (the difference in stripping between the hydrodynamical and DMO simulations) gives a value of 0.82 for the ratio of the mass functions, corresponding to an 18% reduction in the number of objects. This stripping effect is the dominant cause for the reduction in subhalo abundance for distances greater than 200 kpc from the centre of the halo. Stronger stripping in the hydrodynamical simulations also explains why the orange points (i.e. with corrected masses) in Fig. 9 lie slightly below the 1:1 line on average.

Finally, in Fig. 11 we show the reduction in subhalo abundance in the hydrodynamical relative to the DMO versions of the AURIGA simulations out to a radius of 800 kpc. Each line gives the median reduction in subhalo abundance in a given mass bin for the six high-resolution AURIGA halos. In this case we multiplied the masses of DMO subhalos by 0.75 following the method described in §2.2. We see a clear change in gradient around 300 kpc from the main halo. Inside this distance the reduction in abundance decreases approximately linearly with radius. Even at distances of 400 kpc or greater from the halo, the ratio of number densities has not yet reached unity. This is partly a result of the inability of our mass correction to capture the full range of different growth histories of subhalos in the DMO and hydrodynamical simulations, and partly a result of the same processes that destroy subhalos near the centre of the main halo being played out in smaller halos that later merge into the main one. For the AURIGA suite of simulations there are, on average, 3 galaxies with stellar mass greater than 10^8 $M_\odot$ between 400 and 800 kpc from the centre of the main halo, as well as dozens of smaller galaxies. The presence of massive galaxies (and their more disruptive tidal forces) at the centre of all these halos/subhalos will also contribute in a small way to the reduction

Downloaded from https://academic.oup.com/mnras/advance-article-abstract/doi/10.1093/mnras/stz3448/5679897 by University of Durham user on 03 January 2020

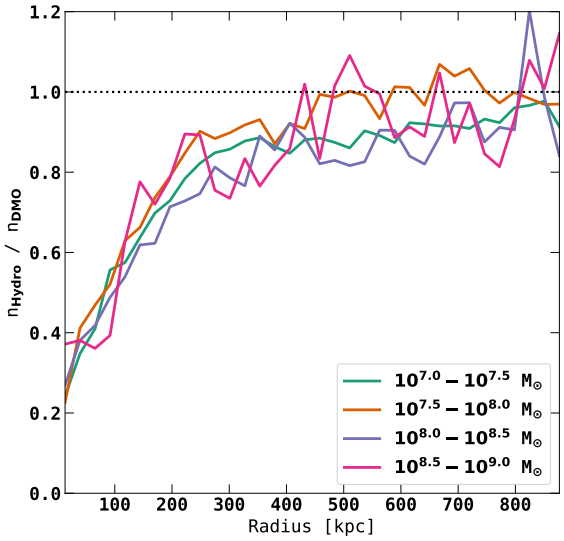

Figure 11. The ratio of the radial number density of subhalos in hydrodynamical to DMO versions of the AURIGA simulations. Each line represents a different mass bin as indicated in the legend. The results are time-averaged over a period of 5 Gyr. The masses of subhalos used in this figure are the "effective" masses, calculated using the method described in §2.2.

in the abundance of substructure relative to the DMO version of the simulations.

3.2 The SUBFIND algorithm

Halo substructure in the APOSTLE and AURIGA simulations is identified using the SUBFIND algorithm (Springel et al. 2001). The SUBFIND algorithm identifies subhalos by selecting a list of particles inside locally overdense regions, and then removing particles from this list based on their binding energy. The mass of a subhalo as calculated by the SUBFIND algorithm therefore depends upon the local environment of the subhalo. Near the centre of a large halo, the reported mass of a subhalo will be lower than if the same set of particles were analysed at a greater distance from the halo centre.

Here we consider whether this radial-dependent property of the SUBFIND algorithm will affect our comparison of substructure properties in hydrodynamical and DMO simulations. In the simulations we study, DMO halos and subhalos tend to be around 25% more massive than their hydrodynamical counterparts (as discussed in §2.2). It is important to know whether this systematic difference in mass, coupled with the radial bias of the SUBFIND algorithm and the slight differences in resolution between the APOSTLE and AURIGA simulations, could be a contributing factor to the differences observed between the simulations.

To shed light on this issue, we perform the following test. We create an idealised NFW halo using 5×10^7 particles, with M_{200}= 10^{12} M$_\odot$ and a concentration of $c = 10$, a typical value for halos of this mass[4]. We then create a smaller NFW halo, with a concentration of $c = 20$, whose particles have the same mass as the particles in the larger NFW halo. We then implant the smaller halo inside the larger, at various distances from the centre of the larger halo. For each placement of the smaller halo, we run the SUBFIND algorithm on the total set of particles. This procedure was repeated for subhalos with different numbers of particles. We take the NFW distribution function to be a function of energy only, and set the velocities of individual particles accordingly. We do not add a bulk velocity to the test subhalo. We have checked and found the difference in identified mass of stationary and fast moving subhalos is negligible compared to the size of the other effects discussed in this section.

The results of this test are shown in Fig. 12. We see a clear trend in the reduction of the calculated subhalo mass as the local density increases (i.e. at smaller radii). An increase in the local density of approximately three orders of magnitude leads to a reduction in the reported SUBFIND mass by a factor of ten. The comparatively small differences in local density between the simulations considered means that the density dependence of the SUBFIND algorithm does not contribute significantly to the results presented in this section.

The size of this effect does not depend strongly on subhalo mass, except for cases in the very centre of the halo where the SUBFIND algorithm fails to even identify the existence of the smallest halo tested. Since the effect of radius on reported mass is approximately the same for subhalos with masses spanning two orders of magnitude, we do not expect that the behaviour of the SUBFIND algorithm has a significant impact on the results presented in this section, where the mass differences are much smaller. Our one caveat applies to the least massive subhalos in our simulations. It is probable that our sample of subhalos is incomplete for radial distances of less than roughly 10 kpc. Since the majority of substructure observed at small radii is only observed due to the orbit integration method we employ, the effect of the radial dependence of the SUBFIND algorithm on our results is small.

We also quantify this radial effect on the quantity $V_{\rm max}$, the maximum value of a subhalo's rotation curve. The radial dependence of the calculated $V_{\rm max}$ is much weaker than for the total subhalo mass. This is because the value of $V_{\rm max}$ depends on the innermost particles, whereas the outermost particles in our idealised subhalos are the ones most likely to be identified as belonging to the host halo.

4 SUBHALO VELOCITIES

An accurate estimate of the expected velocity distribution of low mass substructures is a critical input into methods to search for small-mass dark substructures from measured gaps in cold stellar streams. In this section we examine the velocity distributions in our simulations; contrasting the two sets, we can gain some insight into the size of the theoretical uncertainties in these distributions. This topic has been explored already by, for example, Sawala et al. (2017).

To obtain a robust estimate of the velocity distributions, we employ kernel-density estimation (Rosenblatt 1956; Parzen 1962), using a Gaussian kernel and applying Scott's rule to estimate the bandwidth (Scott 2015). The distribution of subhalo speeds as a function of radius is shown in Fig. 13. The presence of the central galaxy affects the distributions relative to the DMO case for both hydrodynamical sets of simulations. The impact of the more massive central galaxies in the AURIGA simulations is clear. The depth of the potential well is larger, leading to a greater radial acceler-

[4] We create this halo using the publicly available code PYICS, described in (Herpich et al. 2017), which is in turn based on the algorithm introduced by Kazantzidis et al. (2004).

Downloaded from https://academic.oup.com/mnras/advance-article-abstract/doi/10.1093/mnras/stz3448/5679897 by University of Durham user on 03 January 2020

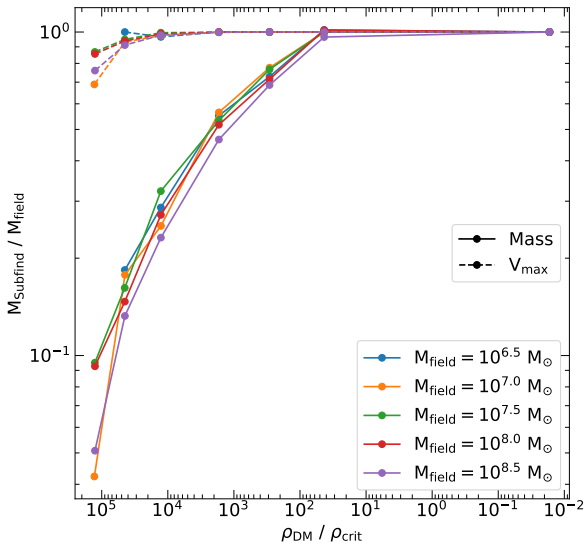

Figure 12. The ratio of subhalo mass/$V_{\rm max}$ to the field mass/$V_{\rm max}$ of the same set of particles, as calculated by the SUBFIND algorithm, as a function of the local matter density. The field mass is defined as the mass reported by the SUBFIND algorithm when the subhalo is placed far from the edge of the parent halo. Solid lines show the reduction in subhalo mass, whilst dashed lines show the reduction in $V_{\rm max}$.

	0-10	10-20	20-50	50-200
Apostle DMO	351, 110	310, 101	242, 97	167, 78
Auriga DMO	384, 68	355, 66	285, 75	191, 71
Apostle Hydro	379, 75	326, 83	249, 81	165, 71
Auriga Hydro	554, 48	480, 43	356, 56	211, 63

Table 3. Values of the parameters ν and σ obtained from fitting a Rician distribution to the median values of the velocity distributions shown in Fig. 13, in km/s. Each column correspond to a different radial bin, with the width of the shell in kiloparsecs.

ation as subhalos fall inwards. This effect of the central galaxy is also manifest in the APOSTLE simulations but it is much weaker reflecting the smaller masses of the central galaxies. We note that no such effect was observed by Sawala et al. (2017), probably as result of inaccuracies in their interpolation scheme.

We find that the distribution of subhalo speeds is generally well fit by a Rician distribution, in agreement with Sawala et al. (2017). The Rician distribution is a two-parameter model given by

$$f(x \mid \nu, \sigma) = \frac{x}{\sigma^2} \exp\left(\frac{-(x^2+\nu^2)}{2\sigma^2}\right) I_0\left(\frac{x\nu}{\sigma^2}\right), \qquad (4)$$

where I_0 is the modified Bessel function of the first kind with order zero. The ν parameter controls the location of the peak, with a value of 0 giving a Maxwellian distribution. The σ parameter controls the width of the distribution. The parameters of the fits are given in Table 3.

The distributions of subhalo *radial* velocities in the same radial bins used in Fig. 13 are shown in Fig. 14. Sawala et al. (2017) found that close to the halo centre, the distribution of subhalo radial velocities in the Apostle simulations was well described by a double Gaussian. Fig. 4 shows how plunging orbits calculated using the cubic spline interpolation method pass closer to the centre of the halo than the true orbits, with a velocity that is predominantly tangential during most of the passage through the central region. This is a general feature of orbits constructed using the cubic spline interpolation method. Consequently, the dearth of low-radial velocity orbits reported by Sawala et al. (2017) is an artifact of their orbit reconstruction method. This explains why the velocity distributions that we find in the top left panel of Fig. 14 do not show such a pronounced dip around $v_{\rm rad} = 0$. In the 50–200 kpc radial bins, we see that one of the AURIGA systems has an unusually bimodal velocity distribution. This distribution is the result of an interaction with another halo between redshift $z = 0.5$ and the present day. A population of subhalos belonging to the passing halo have flown in and out of the edge of the halo, resulting in a peak of the negative radial velocity whilst infalling, and a peak in the positive radial velocity distribution after pericentre.

We can see in Fig. 14 that the deeper gravitational potential the in hydrodynamical simulations relative to the DMO case leads to a broadening of the radial velocity distribution, with the effect being most pronounced in the AURIGA simulations at small radii. This effect is a combination of a greater radial acceleration and the preferential disruption of objects on more circular orbits near the centre of the halo. We also note that the distributions are remarkably symmetrical, even in the outermost spherical shell. This shows that the subhalo abundance at all radii reflects a balance between inflow and outflow.

5 CONCLUSIONS

The large number of low-mass halos predicted by N-body simulations to form in a ΛCDM universe provide a key test of the paradigm. In practice, however, the clear-cut predictions from N-body simulations are only part of the answer, as some of these small halos that fall into larger ones can be destroyed by tidal forces whose strength depends on the contents of the halo, particularly the galaxy at the centre. Thus, rigorous predictions for the abundance of subhalos requires modelling the baryonic processes that lead to the formation of the galaxy. In this paper, we have investigated how the abundance and velocity distribution of small-mass subhalos ($\sim 10^{6.5} - 10^{8.5} {\rm M}_\odot$) within galaxy-size halos is affected by baryon processes and we have compared two different implementations of such processes using the independent APOSTLE and AURIGA simulations.

Since subhalos are quite rare near the centre of the host halo and are poorly sampled in the limited number of available simulation outputs, to study their orbits we have integrated the orbits of subhalos between snapshots, using the publicly available code GALPY. The results we present are obtained by averaging over a lookback period of 5 Gyr.

We find that the abundance of substructures is significantly affected by the way in which baryon processes are treated. At 10% of r_{200} the abundance of low-mass substructures is reduced relative the dark matter-only (DMO) simulations by around 50% and 80% in the APOSTLE and AURIGA simulations respectively. We also find differences in the slope of the subhalo mass function and the width and peak location of the velocity distributions, all of which can be explained by the different masses of the galaxies that form at the centre of the halos in the two simulations. The more massive central galaxies in AURIGA result in larger tidal forces, which cause enhanced destruction and stripping of substructures. Perhaps surprisingly, we find that the abundance of subhalos in the hydrodynamical simulations is still lower than in the DMO simulations

Downloaded from https://academic.oup.com/mnras/advance-article-abstract/doi/10.1093/mnras/stz3448/5679897 by University of Durham user on 03 January 2020

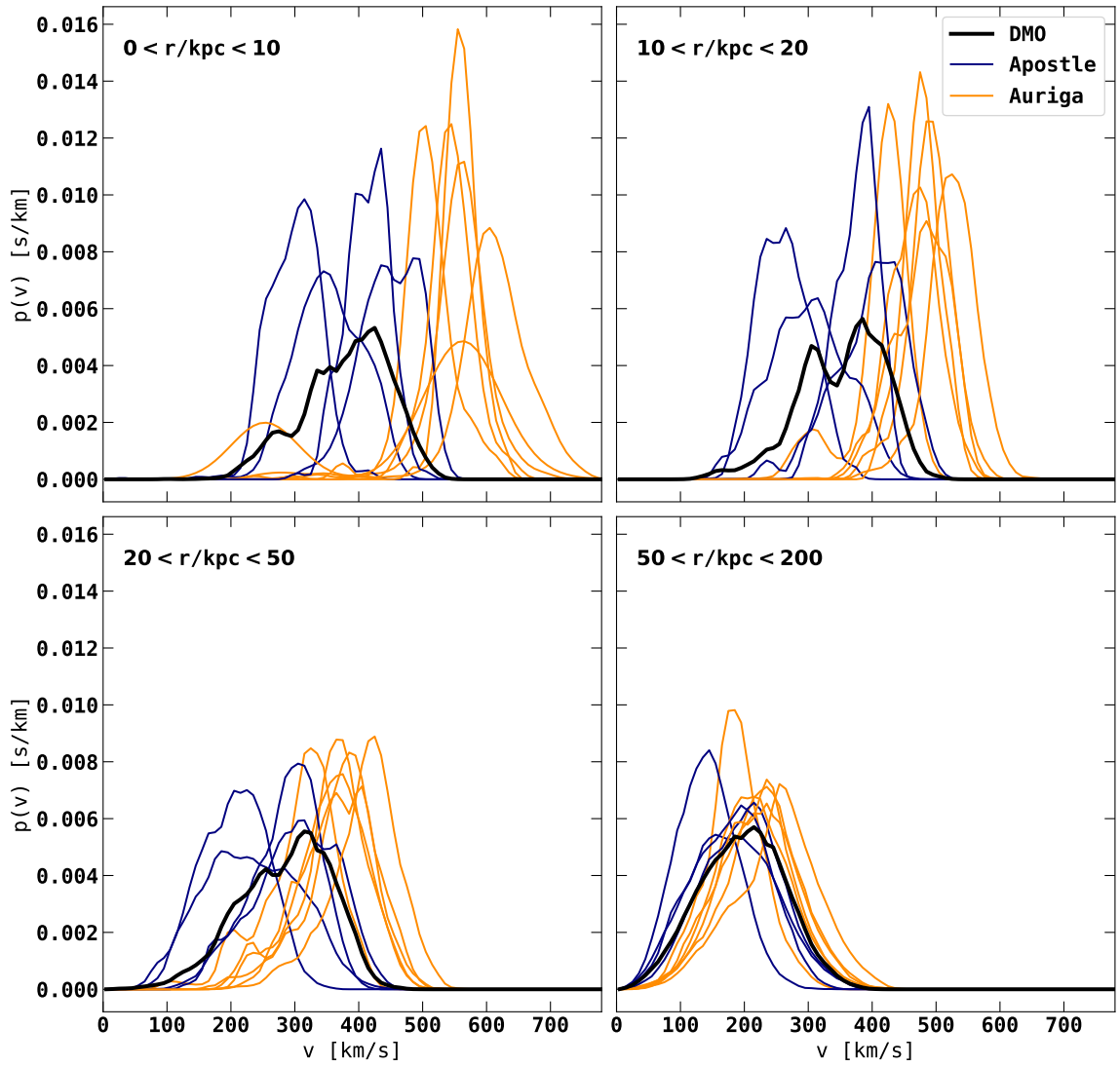

Figure 13. Probability distributions of the speed (relative to the host halo) in spherical shells for subhalos of mass in the range $(10^{6.5} - 10^{8.5})$ $M_\odot$ in the APOSTLE (blue) and AURIGA (orange) simulations. Thick black lines show the median velocity distribution of all DMO subhalos in each bin.

even well beyond r_{200}, particularly in AURIGA. This happens because objects that spend the majority of their orbit far from the central galaxy have highly radial orbits which take them past r_{200}; some of the objects that emerge unscathed from the DMO simulation, are destroyed in the hydrodynamical counterpart.

A deeper potential also causes subhalos to accelerate more as they move towards the centre of the halo, leading to an increase in the width of the radial velocity distributions. We also find that the peak of the distribution of subhalo speeds is shifted to significantly higher values in the hydrodynamical simulations, with the largest changes occurring near the centre of the AURIGA simulations.

Sawala et al. (2017) and Garrison-Kimmel et al. (2017) investigated similar processes to those we have studied here, the former using the same APOSTLE simulations that we too have analyzed. Our results differ significantly from theirs. We have shown that this is because the cubic spline method they used to interpolate orbits between snapshots is insufficiently accurate to follow the orbits near the centre of the halo. Our orbit integration method predicts less substructure at small distances from the halo centre. We also do not observe the velocity biases described by Sawala et al. (2017). However, we find that the conclusion of Sawala et al. (2017) that

Downloaded from https://academic.oup.com/mnras/advance-article-abstract/doi/10.1093/mnras/stz3448/5679897 by University of Durham user on 03 January 2020

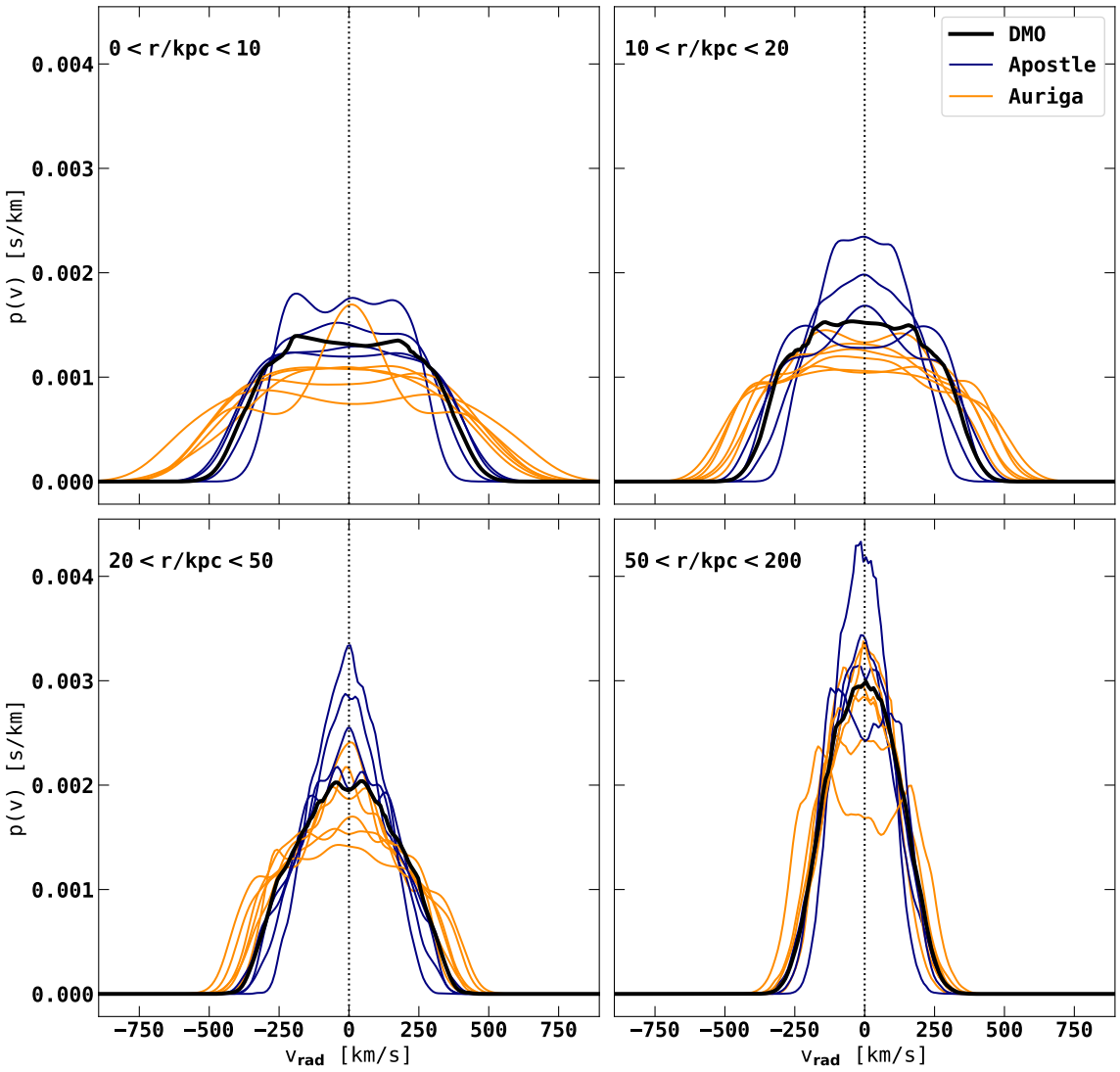

Figure 14. Probability distributions of radial velocities (relative to the host host halo) in spherical shells for subhalos with masses in the range $(10^{6.5} - 10^{8.5})$ $\mathrm{M}_\odot$ in the APOSTLE (blue) and AURIGA (orange) simulations. Thick black lines show the median velocity distribution of all DMO subhalos in each bin.

objects on radial orbits are more likely to undergo disruption by the central galaxy holds true.

Roughly speaking the APOSTLE and AURIGA simulations bracket the range of theoretical uncertainty for the abundance and velocity distribution of substructures near the centre of a galaxy like the Milky Way. APOSTLE underpredicts the mass of the Milky Way by factors of 2-3, whereas, on average, the AURIGA galaxies overpredict it by factors of 1.5-2. The halo-to-halo variations in the velocity distributions is smaller than the differences seen in our two hydrodynamical simulations. This size of theoretical uncertainty is eminently reducible by improved modelling of the baryonic physics of galaxy formation.

6 ACKNOWLEDGEMENTS

CSF acknowledges support from European Research Council (ERC) Advanced Investigator grant DMIDAS (GA 786910). KO received support from VICI grant 016.130.338 of the Netherlands Foundation for Scientific Research (NWO). This work was also supported by the Consolidated Grant for Astronomy at Durham

Downloaded from https://academic.oup.com/mnras/advance-article-abstract/doi/10.1093/mnras/stz3448/5679897 by University of Durham user on 03 January 2020

(ST/L00075X/1). It made use the DiRAC Data Centric system at Durham University, operated by the Institute for Computational Cosmology on behalf of the STFC DiRAC HPC Facility (www.dirac.ac.uk). This equipment was funded by BIS National E-infrastructure capital grant ST/K00042X/1, STFC capital grants ST/H008519/1 and ST/K00087X/1, STFC DiRAC Operations grant ST/K003267/1 and Durham University. DiRAC is part of the National E-Infrastructure.

REFERENCES

Anderson M. E., Churazov E., Bregman J. N., 2015, MNRAS, 452, 3905
Benitez-Llambay A., Frenk C. S., Ludlow A. D., Navarro J. F., 2018, arXiv e-prints, p. arXiv:1810.04186
Benson A. J., Frenk C. S., Sharples R. M., 2002, ApJ, 574, 104
Bose S., et al., 2017, MNRAS, 464, 4520
Bovy J., 2015, ApJS, 216, 29
Boyarsky A., Ruchayskiy O., Iakubovskyi D., Franse J., 2014, Physical Review Letters, 113, 251301
Boylan-Kolchin M., Bullock J. S., Kaplinghat M., 2011, MNRAS, 415, L40
Bulbul E., Markevitch M., Foster A., Smith R. K., Loewenstein M., Randall S. W., 2014, ApJ, 789, 13
Bullock J. S., Kravtsov A. V., Weinberg D. H., 2000, ApJ, 539, 517
Carlberg R. G., Grillmair C. J., Hetherington N., 2012, ApJ, 760, 75
Colín P., Avila-Reese V., Valenzuela O., 2000, ApJ, 542, 622
Crain R. A., et al., 2015, MNRAS, 450, 1937
D'Onghia E., Springel V., Hernquist L., Keres D., 2010, ApJ, 709, 1138
Davis M., Efstathiou G., Frenk C. S., White S. D. M., 1985, ApJ, 292, 371
Despali G., Vegetti S., 2017, MNRAS, 469, 1997
Despali G., Vegetti S., White S. D. M., Giocoli C., van den Bosch F. C., 2018, MNRAS, 475, 5424
Diemand J., Kuhlen M., Madau P., 2007, ApJ, 667, 859
Erkal D., Belokurov V., 2015a, MNRAS, 450, 1136
Erkal D., Belokurov V., 2015b, MNRAS, 454, 3542
Erkal D., Belokurov V., Bovy J., Sanders J. L., 2016, MNRAS, 463, 102
Errani R., Peñarrubia J., Laporte C. F. P., Gómez F. A., 2017, MNRAS, 465, L59
Fattahi A., et al., 2016, MNRAS, 457, 844
Franse J., et al., 2016, ApJ, 829, 124
Garrison-Kimmel S., et al., 2017, MNRAS, 471, 1709
Ghigna S., Moore B., Governato F., Lake G., Quinn T., Stadel J., 1998, MNRAS, 300, 146
Gill S. P. D., Knebe A., Gibson B. K., 2005, MNRAS, 356, 1327
Gilmore G., et al., 2012, The Messenger, 147, 25
Grand R. J. J., Springel V., Gómez F. A., Marinacci F., Pakmor R., Campbell D. J. R., Jenkins A., 2016, MNRAS, 459, 199
Hellwing W. A., Frenk C. S., Cautun M., Bose S., Helly J., Jenkins A., Sawala T., Cytowski M., 2016, MNRAS, 457, 3492
Herpich J., Stinson G. S., Rix H.-W., Martig M., Dutton A. A., 2017, MNRAS, 470, 4941
Hui L., Ostriker J. P., Tremaine S., Witten E., 2017, Phys. Rev. D, 95, 043541
Jeltema T., Profumo S., 2015, MNRAS, 450, 2143
Kazantzidis S., Magorrian J., Moore B., 2004, ApJ, 601, 37
Klypin A., Kravtsov A. V., Valenzuela O., Prada F., 1999, ApJ, 522, 82
Koopmans L. V. E., 2005, MNRAS, 363, 1136
LSST Science Collaboration et al., 2009, preprint, (arXiv:0912.0201)
Li R., Frenk C. S., Cole S., Gao L., Bose S., Hellwing W. A., 2016, MNRAS, 460, 363
Li R., Frenk C. S., Cole S., Wang Q., Gao L., 2017, MNRAS, 468, 1426
Lovell M. R., et al., 2012, MNRAS, 420, 2318
Lovell M. R., Gonzalez-Perez V., Bose S., Boyarsky A., Cole S., Frenk C. S., Ruchayskiy O., 2017, MNRAS, 468, 2836
Lowing B., Jenkins A., Eke V., Frenk C., 2011, MNRAS, 416, 2697
Macciò A. V., Kang X., Fontanot F., Somerville R. S., Koposov S., Monaco P., 2010, MNRAS, 402, 1995
Malyshev D., Neronov A., Eckert D., 2014, Phys. Rev. D, 90, 103506
Moore B., Ghigna S., Governato F., Lake G., Quinn T., Stadel J., Tozzi P., 1999, ApJ, 524, L19
Okamoto T., Gao L., Theuns T., 2008, MNRAS, 390, 920
Parzen E., 1962, Ann. Math. Statist., 33, 1065
Peebles P. J. E., 1980, The large-scale structure of the universe
Perryman M. A. C., et al., 2001, A&A, 369, 339
Petraki K., Volkas R. R., 2013, International Journal of Modern Physics A, 28, 1330028
Planck Collaboration et al., 2016, A&A, 596, A108
Pontzen A., Roškar R., Stinson G. S., Woods R., Reed D. M., Coles J., Quinn T. R., 2013, pynbody: Astrophysics Simulation Analysis for Python
Riemer-Sørensen S., 2016, A&A, 590, A71
Rosenblatt M., 1956, Ann. Math. Statist., 27, 832
Sawala T., Frenk C. S., Crain R. A., Jenkins A., Schaye J., Theuns T., Zavala J., 2013, MNRAS, 431, 1366
Sawala T., et al., 2016, MNRAS, 457, 1931
Sawala T., Pihajoki P., Johansson P. H., Frenk C. S., Navarro J. F., Oman K. A., White S. D. M., 2017, MNRAS, 467, 4383
Schaye J., et al., 2015, MNRAS, 446, 521
Schewtschenko J. A., Wilkinson R. J., Baugh C. M., Bœhm C., Pascoli S., 2015, MNRAS, 449, 3587
Schneider A., Smith R. E., Macciò A. V., Moore B., 2012, MNRAS, 424, 684
Scott D., 2015, Multivariate Density Estimation: Theory, Practice, and Visualization, 2 edn. Wiley
Somerville R. S., 2002, ApJ, 572, L23
Spergel D. N., Steinhardt P. J., 2000, Physical Review Letters, 84, 3760
Springel V., 2011, in Alves J., Elmegreen B. G., Girart J. M., Trimble V., eds, IAU Symposium Vol. 270, Computational Star Formation. pp 203–206, doi:10.1017/S1743921311000378
Springel V., White S. D. M., Tormen G., Kauffmann G., 2001, MNRAS, 328, 726
Springel V., et al., 2008, MNRAS, 391, 1685
The Dark Energy Survey Collaboration 2005, ArXiv Astrophysics e-prints,
Vegetti S., Lagattuta D. J., McKean J. P., Auger M. W., Fassnacht C. D., Koopmans L. V. E., 2012, Nature, 481, 341
Vogelsberger M., et al., 2014, Nature, 509, 177
Yurin D., Springel V., 2015, MNRAS, 452, 2367

Downloaded from https://academic.oup.com/mnras/advance-article-abstract/doi/10.1093/mnras/stz3448/5679897 by University of Durham user on 03 January 2020